

Entropy-driven formation of large icosahedral colloidal clusters by spherical confinement

Supplementary information

Bart de Nijs ^{1†}, Simone Dussi ^{1†}, Frank Smalenburg ¹, Johannes D. Meeldijk ², Dirk J. Groenendijk ¹, Laura Filion ¹, Arnout Imhof ¹, Alfons van Blaaderen ^{1*}, Marjolein Dijkstra ^{1*}

¹Soft Condensed Matter, Debye Institute for Nanomaterials Science, Utrecht University, Princetonplein 5, 3584 CC Utrecht, The Netherlands

²Electron Microscopy Group, Utrecht University, Padualaan 8, 3584 CH Utrecht, The Netherlands

† These authors contributed equally to this work.

* To whom correspondence should be addressed.
E-mail: M.Dijkstra1@uu.nl ; A.vanBlaaderen@uu.nl

Supplementary Methods

Chemicals

All chemicals were used as received. Chemicals used were dextran from *Leuconostoc mesenteroides* (Sigma Aldrich, mol. wt. 1.500.000 - 2.800.000), cyclohexane (Sigma Aldrich, $\geq 99.8\%$), sodium dodecyl sulfate (SDS, Sigma Aldrich, $\geq 99.0\%$), toluene (Acros, $\geq 99.7\%$), 1-hexadecene ($\geq 99\%$), hexadecane (Sigma Aldrich, $\geq 99\%$), Span 80 (Sigma Aldrich), oleic acid (Sigma Aldrich, $\geq 90\%$), Fluorescein isothiocyanate (Sigma Aldrich, isomer I, FITC, $\geq 90\%$), ethanol (Baker Analyzed, $\geq 99.9\%$, absolute). For de-ionized water a Millipore Direct-Q UV3 reverse osmosis filter apparatus was used ($18\text{ M}\Omega$ at $25\text{ }^\circ\text{C}$).

Equipment

For electron tomography a FEI Tecnai 20 electron microscope was used with a LaB₆ tip at an accelerating voltage of 200 kV in bright field mode. Transmission electron microscopy (TEM) was performed on a FEI Tecnai 12 with a tungsten tip, operating at 120 kV . For scanning transmission electron microscopy (STEM) a FEI Tecnai 20F with a Field Emission Gun (FEG) was used, operating at 200 kV in secondary electron mode (SE-STEM) or in high-angle annular dark-field mode (HAADF-STEM). Confocal analysis was performed on a Leica SP2 confocal microscope with an $100\times$ ($\text{NA} = 1.4$) oil immersion Leica confocal objective. For centrifugation of nanoparticles a Hettich zentrifugen Rotina 46 S @ 4000 RPM was used, while for centrifugation of nanoparticle clusters an Eppendorf centrifuge 5415c was used @ 1000 RPM .

Synthesis of cobalt iron oxide and core-shell semiconductor nanoparticles

6.0 nm cobalt iron oxide nanoparticles with an oleic acid capping were synthesized according to the method described by Bodnarchuk *et al.* (1), using hexadecene as solvent instead of octadecene, and washed three times using ethanol/cyclohexane (1:1 v/v) by sedimenting and redispersing using centrifugation. Electron microscopy analysis showed nanoparticles with a 6.0 nm core with a standard deviation of 0.3 nm resulting in a polydispersity of 4.8% . The effective diameter was found to be 9.0 nm as a result of the oleic acid ligand molecules (measured over multiple particles in close packed structures). This resulted in an effective polydispersity of 3.2% (see Supplementary Fig. 1 left).

For experiments on core-shell semiconductor nanoparticles, 12.4 nm CdSe@ZnS

multishell nanoparticles with a polydispersity of 8.1 % were used, synthesized according to Xie *et al.* (2). These particles were capped with oleic acid resulting in an effective diameter of 14.5 nm and an effective polydispersity of 6.9 % (see Supplementary Fig. 1 right).

Synthesis of silica colloids

Fluorescent core-shell particles were made using the dye fluorescein isothiocyanate (FITC) according to the method by van Blaaderen *et al.* (3). The cores had a diameter of 434 nm and were used in seeded growth to arrive at a final diameter of 1.32 μm . Successive silica shells were grown on the cores according to the Giesche method (4). Electron microscopy analysis showed silica colloids with a diameter of 1.32 μm with a polydispersity of 1.7 % (see Supplementary Fig. 2).

Experimental self-assembly in spherical confinement

For a typical nanoparticle self-assembly experiment 5 mg of 6.0 nm cobalt iron oxide nanoparticles were dispersed in 1 ml of cyclohexane and added to a mixture of 800 mg of dextran and 120 mg of sodium dodecyl sulfate in 20 ml of de-ionized water. The resulting emulsion was agitated by shear with a shear rate of $\dot{\gamma} = 1.56 \times 10^5 \text{ s}^{-1}$, using a Couette rotor-stator device (gap spacing 0.1 mm) following the procedure and equipment described by Mason and Bibette (5). The emulsion was then heated to 68 °C and kept at this temperature for 4 hours to evaporate the inner cyclohexane phase. The suspension was then allowed to cool to room temperature. The resulting supraparticle suspension was washed twice, sedimenting and redispersing in de-ionized water. Examples of nanoparticle clusters are shown in Supplementary Fig. 1 and additional images of a FCC supraparticle are shown in Supplementary Fig. 3.

Self-assembly experiments were also performed with semiconductor nanoparticles yielding similar results as the cobalt iron oxide nanoparticles, as shown in Supplementary Fig. 4. For a typical self-assembly experiment 5 mg of semiconductor nanoparticles were dispersed in 1 ml of cyclohexane. Consecutively, the same steps were performed as described for the cobalt iron oxide nanoparticle self-assembly experiments. After self-assembly, bright red photoluminescent supraparticles were observed with a peak in intensity at the same wavelength ($\lambda_{\text{max}} = 650 \text{ nm}$) as for the constituent nanoparticles.

For a typical colloidal self-assembly experiment 5 mg of silica colloids were dispersed in 25 μL of de-ionized water. The suspension was then added to 150 μL of hexadecane containing 1.5 mg Span 80. The suspension was shaken slightly by hand. The inner water phase of the emulsion droplets was allowed to evaporate over 10 days with slight agitation (shaking) every 48 hours to prevent droplets

from sticking to the glass vial. The resulting suspension was washed by sedimenting and redispersing in water. Images of typical colloidal clusters are shown in Supplementary Fig. 5.

Electron microscopy sample preparation

To prepare sample for electron microscopy, 16 nm gold nanoparticles were deposited (from ethanol) on the transmission electron microscopy (TEM) grid prior to the sample deposition. These functioned as fiducial markers for tomographic reconstruction. 3 μL of the supraparticle suspension in de-ionized water were deposited on the TEM grid and plunge frozen in liquid ethane using a Vitrobot Mark2 plunge freezer. The sample was then freeze-dried over a period of 4 hours under vacuum at $-90\text{ }^\circ\text{C}$ and subsequently allowed to warm to room temperature (RT) prior to TEM analysis.

Scanning transmission electron microscopy analysis

To study the surface order of the nanoparticle supraparticles scanning transmission electron microscopy (STEM) was used operating in secondary electron mode (SE-STEM). To study the interior of the supraparticles, images were acquired in HAADF-STEM mode. Prior to analysis the samples were treated with a plasma cleaner for 2 x 6 seconds to remove excess organic residue. For analysis a Tecnai 20F electron microscope with a FEG was used in STEM mode operating at an accelerating voltage of 200 kV.

Determining nanoparticle and colloid coordinates

The internal structures of nanoparticle assemblies were studied using electron tomography. A Tecnai 20 electron microscope was used with a LaB₆ tip, operating at an accelerating voltage of 200 kV. Tilt series were acquired over 140° using FEI Explore 3D software. The reconstruction was made using IMOD, a software package available via the Boulder Laboratory, Colorado (6, 7). For reconstruction a Simulative Iterative Reconstructive Technique (SIRT) was used with 20 iteration steps.

The orthoslices, from the tomographic reconstruction, were filtered for noise reduction. Using ImageJ, the following filter operations were used: Invert contrast, Subtract background (50 px), a Bandpass filter (30 px high, 3 px low), a Gaussian blur (3 px) and Enhance contrast.

The internal structure of supraparticles consisting of silica colloids was studied using confocal microscopy. For this the supraparticle samples were suspended in an index matching solution of 40/60 hexadecane/toluene inside a capillary. 3D

z -stacks of the colloidal samples were acquired using a Leica SP2 confocal microscope, with a 100x (NA = 1.4) oil objective (see Supplementary Fig. 5).

The tracking software used to find particle positions in both the colloidal and nanoparticle assemblies, was based on the tracking algorithm of Crocker and Grier (8), but extended to 3D as schematically described in (9) (see Supplementary Fig. 6).

In Supplementary Fig. 3 (of the main text), for the surface of the nanoparticles assembly (bottom row, second from the left) we found the particle positions from the SE-STEM image using the 2D tracking shown in Supplementary Fig. 7.

Identifying crystalline domains

We use a local bond orientational order parameter based on spherical harmonics $Y_{l,m}$ to identify the solid-like particles, i.e. particles with a solid-like environment, as introduced in (10). We set $l = 6$, as the face-centered-cubic (FCC) crystal structure is the stable solid phase. Subsequently we use a cluster algorithm (11) to discriminate different crystalline domains.

For each particle i , we calculate

$$q_{6m}(i) = \frac{1}{N_b^i} \sum_{j=1}^{N_b^i} Y_{6,m}(\mathbf{r}_{ij}),$$

where N_b^i is the number of neighbors of particle i , i.e. all particles j with a center-of-mass distance $|r_{ij}| < 1.4\sigma$ with respect to particle i , and σ is the particle diameter. The correlation between two particles i and j is quantified by:

$$d_6(i, j) = \frac{\sum_{m=-6}^{+6} q_{6m}(i)q_{6m}^*(j)}{\left(\sum_{m=-6}^{+6} |q_{6m}(i)|^2\right)^{1/2} \left(\sum_{m=-6}^{+6} |q_{6m}(j)|^2\right)^{1/2}},$$

and for each particle the number of connections is evaluated via

$$n_{con}(i) = \sum_{j=1}^{N_b^i} \mathcal{H}(d_6(i, j) - d_c),$$

where \mathcal{H} is the (Heaviside) step function, and where we fix the correlation threshold $d_c = 0.6$. A particle i is defined as solid-like if $n_{con}(i) \geq 7$.

Different crystal domains are then identified by using an additional constraint to

our criterion, reflecting the fact that the local environment of two neighbouring solid-like particles should display more similarity if they belong to the same crystalline domain than if they are part of different ones. According to this criterion we add particle j (already qualified as a solid-like particle) to the same crystalline domain of particle i if $d_6(i, j) \geq 0.9$.

Molecular dynamics simulations

We perform event-driven molecular dynamics (EDMD) simulations (12) of hard spheres with a diameter σ confined in a spherical cavity. To model the spherical confinement, we use two types of external potentials that act on the hard spheres. In the first case, we treat the confinement as an impenetrable hard spherical wall of radius R . In the second case, we used a soft repulsive wall-particle potential with a functional form $1/|R - r|^n$ with $n \geq 2$, and an interaction range $\leq 2\sigma$, with r the center-of-mass distance of the particle with respect to the center of the cavity. The soft repulsive wall-particle interaction should describe more accurately the deformable emulsion droplet interface compared to the purely hard spherical wall. To mimic the solvent evaporation of the emulsion droplets, the radius of the spherical cavity is slowly reduced at a constant compression speed $v \leq 10^{-4} \sigma/\tau$, where $\tau = \sqrt{m\sigma^2/k_B T}$ is the EDMD time unit, m the mass of a particle, k_B the Boltzmann constant and T the temperature. We use an Andersen thermostat to keep the temperature of the system constant during the simulations.

In addition, we also perform EDMD simulations at fixed density, in which both the number of particles N and the cavity volume V are kept fixed, in order to investigate possible kinetic effects due to the compression. Our results do not alter upon changing the compression speed of the spherical confinement, provided the compression rate is sufficiently slow that the system remains in quasi-equilibrium during the self-assembly process.

Our simulations show clearly that icosahedral ordering arises spontaneously for hard spheres in both a hard and a soft repulsive spherical confinement as shown in Supplementary Fig. 10. Additionally, we clearly observe the structural transition from icosahedral to FCC clusters. We note that the clusters obtained in a soft repulsive spherical confinement have a higher fraction of crystalline particles and a more pronounced icosahedral symmetry than the clusters confined in a hard cavity as the geometrical confinement is less severe for the particles close to the surface, i.e., the clusters become more faceted. Similarly, the anti-Mackay surface termination is also more evident in the case of a soft confinement.

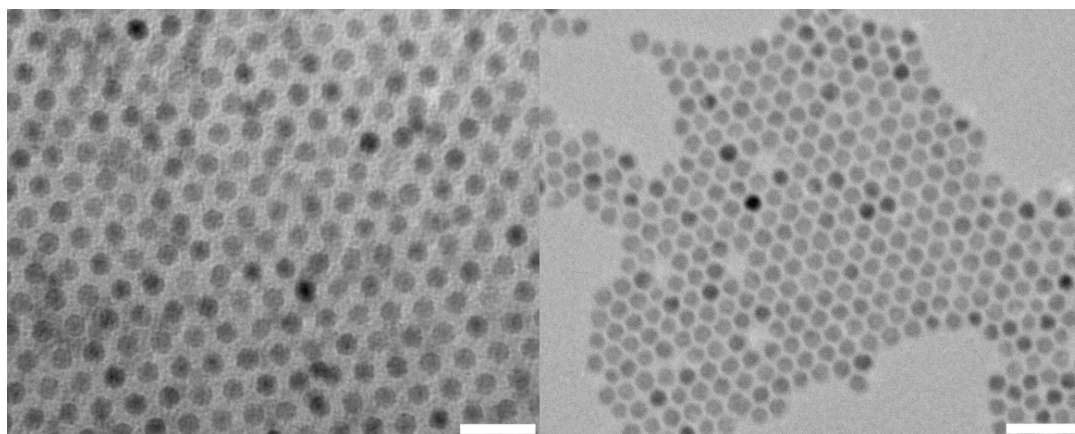
Moreover, we perform simulations with a short-ranged (1σ) attractive potential between interface and particles (maximum depth $10k_B T$). As shown in Supplementary Fig. 11, we can conclude that the type of interface (repulsive or attractive) does not play a vital role in the stabilization of icosahedral symmetry.

Finally, we study the crystallization process using our EDMD simulations. We determine the fraction of crystalline particles in the surface layer near the confining wall, the first three sublayers from the surface, and the inner part of the cavity as a function of packing fraction. In Supplementary Fig. 12, we show results for the formation of a Mackay icosahedral cluster of 2000 hard spheres in a hard spherical confinement. We find that the melting and refreezing of the surface layers is less pronounced than for the anti-Mackay icosahedral cluster as shown in Fig. 4.

Free energy calculations

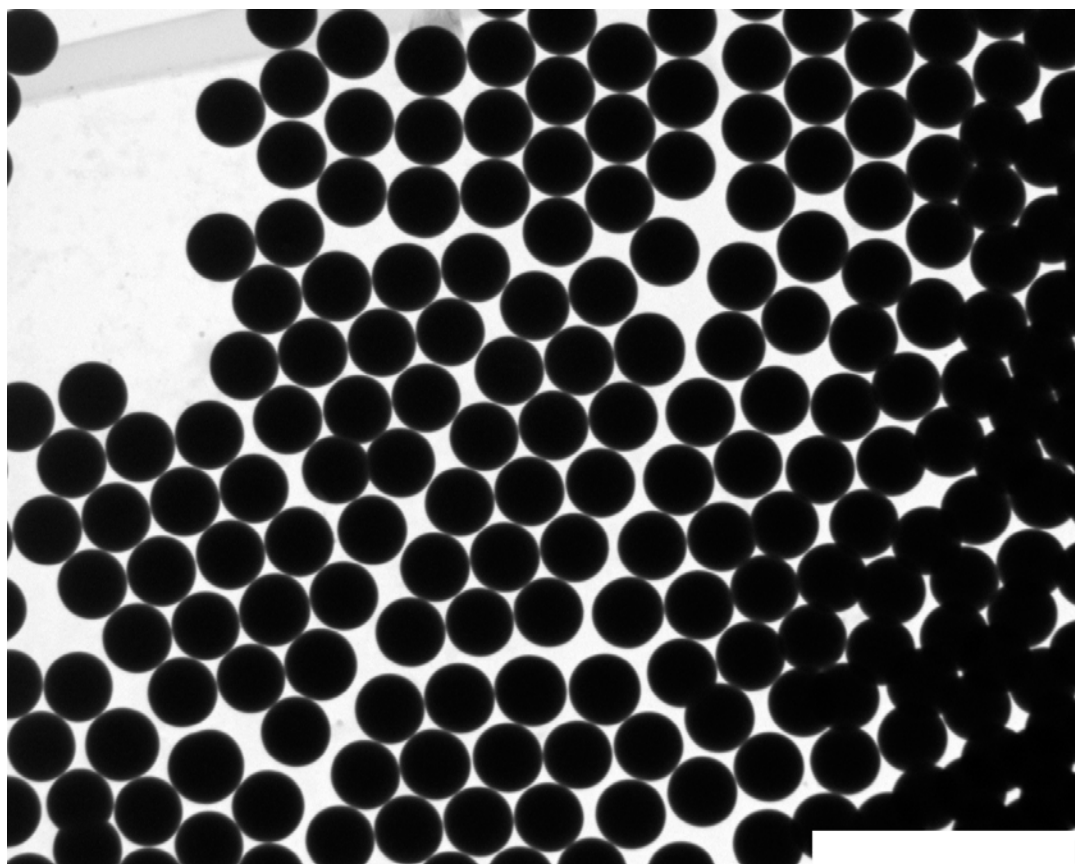
To explore whether the structures we found were equilibrium structures, we calculate the free energy of both FCC clusters as well as icosahedral clusters in a hard spherical cavity using a 3-step thermodynamic integration method proposed by Schilling and Schmid (13). In particular, this method allows us to calculate the free-energy difference between our system, e.g. spherically confined hard spheres, and a reference system for which the free energy is known exactly. The reference system we use consists of non-interacting particles attached, via a linear well potential, to lattice sites. The lattice sites are taken from representative configurations of the system featuring the desired cluster symmetry. In the first integration step, the coupling between the particles and their respective lattice sites is slowly turned on. To accurately perform this integration, we sampled more than 300 values of the coupling constant, and fit the results with an Akima spline before performing the integration. The other two integration steps consist of slowly switching off the hard interactions in the model, i.e. the particle-particle and particle-wall interactions. To do this, we followed the method described in (14). These last two integrations were done using a standard 20-points Gauss-Legendre integration scheme. The results of our free-energy calculations are shown in Supplementary Table 1. They clearly show that for systems with 1500 - 4000 particles, clusters with icosahedral symmetry have lower free energy than the FCC clusters, i.e. are more stable, for the packing fractions we studied. To get an estimate of the error in our free energies, we repeated our calculations on five independent realizations of each cluster geometry.

Supplementary Figures



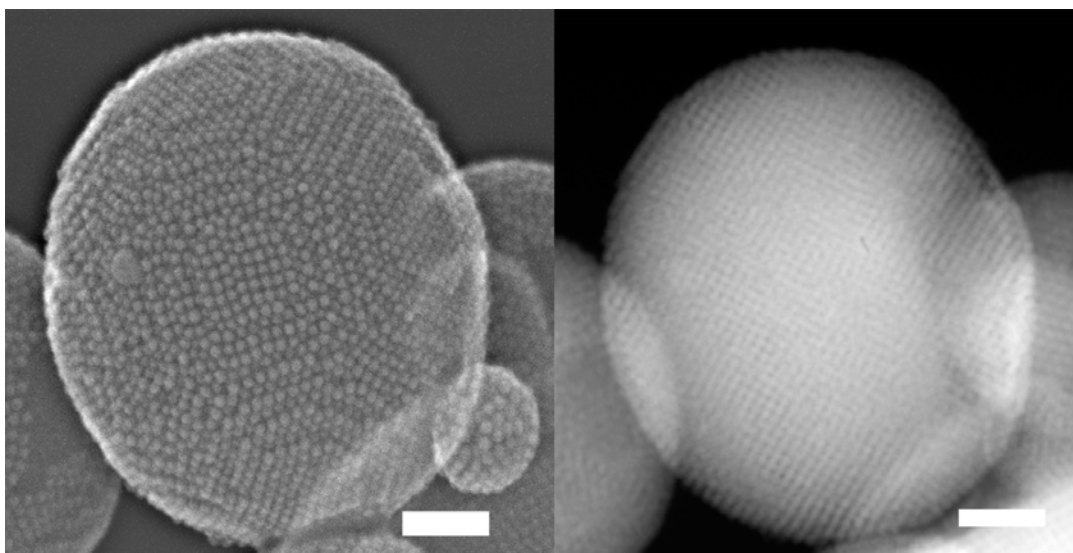
Supplementary Figure 1: Electron micrograph of nanoparticles

Left: Electron micrograph of 6.0 nm cobalt iron oxide nanoparticles with an effective polydispersity of 3.2 % (scalebar = 20 nm). **Right:** Electron micrograph of 12.4 nm CdSe@ZnS semiconductor nanoparticles with an effective polydispersity of 6.9 % (scalebar = 50 nm).



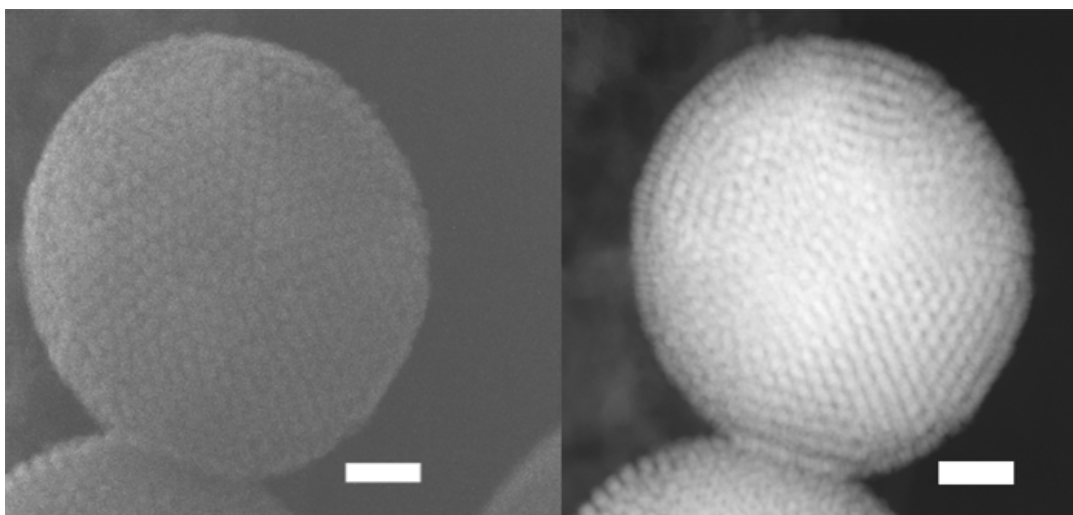
Supplementary Figure 2: Electron micrograph of silica colloids

Electron micrograph of $1.32 \mu\text{m}$ silica colloids with a polydispersity of 1.7 % (scale-bar = $5 \mu\text{m}$).



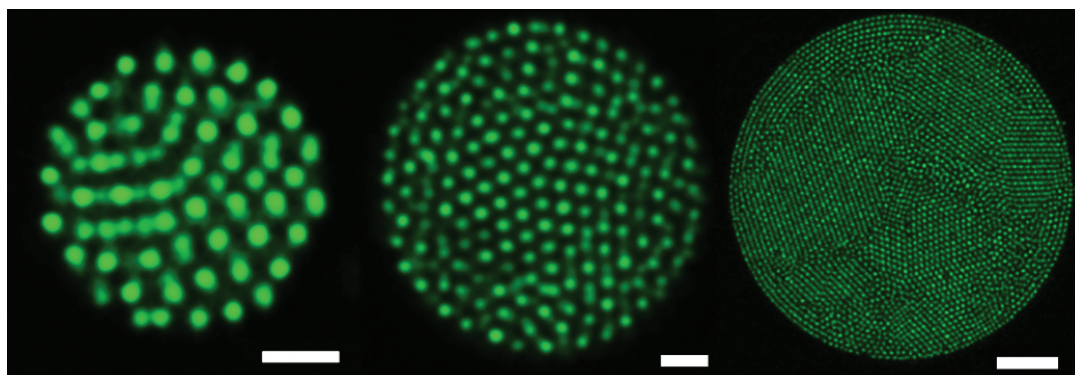
Supplementary Figure 3: Electron micrographs of an FCC supraparticle of cobalt iron oxide nanoparticles

Left: Secondary electron scanning transmission electron microscopy (SE-STEM) image showing a highly ordered surface with hexagonal (111) and square (100) packed domains. The typical step edges are observed. **Right:** HAADF-STEM image showing the highly ordered internal structure of the assemblies with crystallinity throughout.



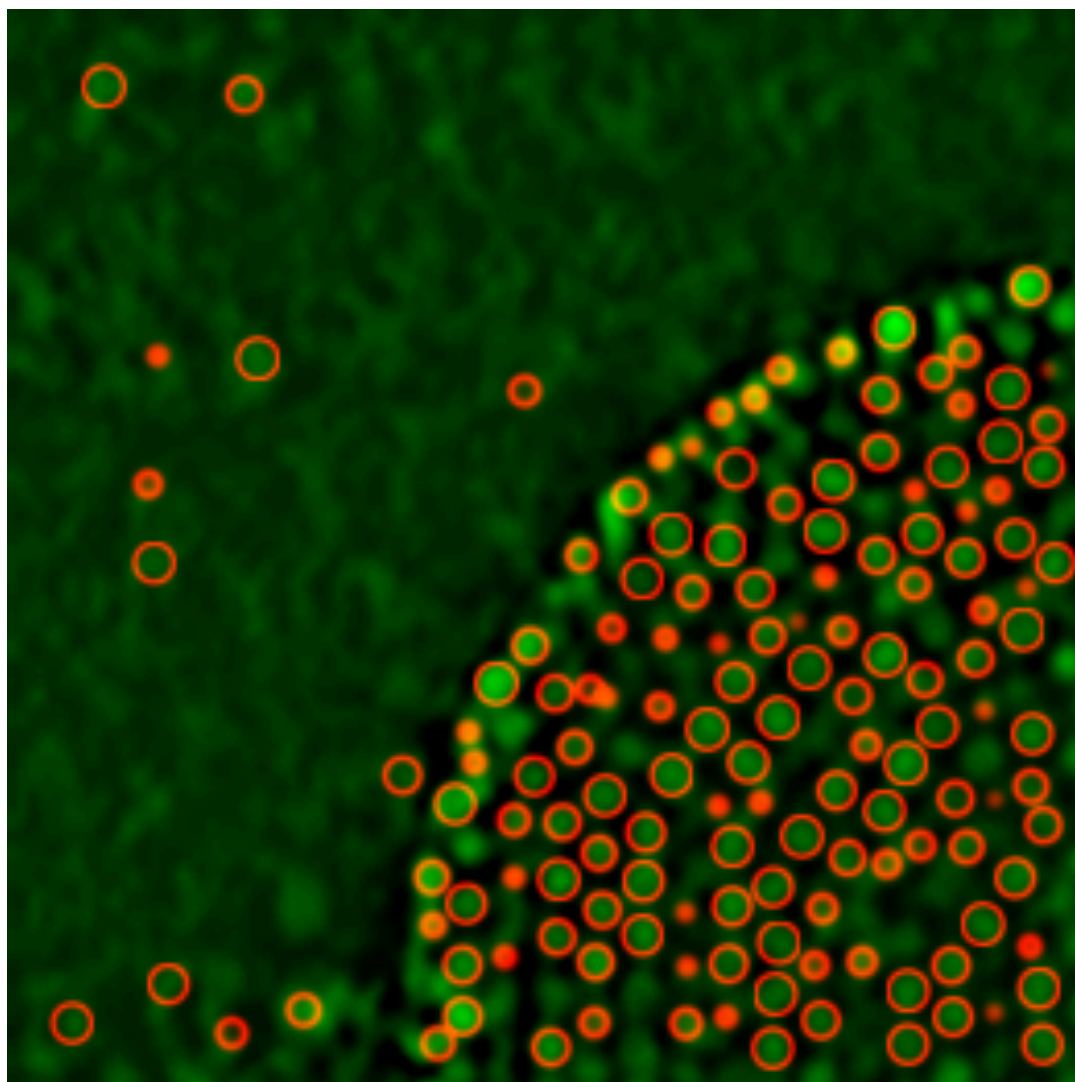
Supplementary Figure 4: Electron micrographs of an icosahedral supraparticle of semiconductor nanoparticles

Similar packing behaviour was observed when CdSe@ZnS core-shell semiconductor nanoparticles were used. **Left:** SE-STEM image of semiconductor nanoparticles self-assembled into a supraparticle. **Right:** HAADF-STEM image of the same supraparticle showing the characteristic wedge shaped domains pointing to the center of the cluster.



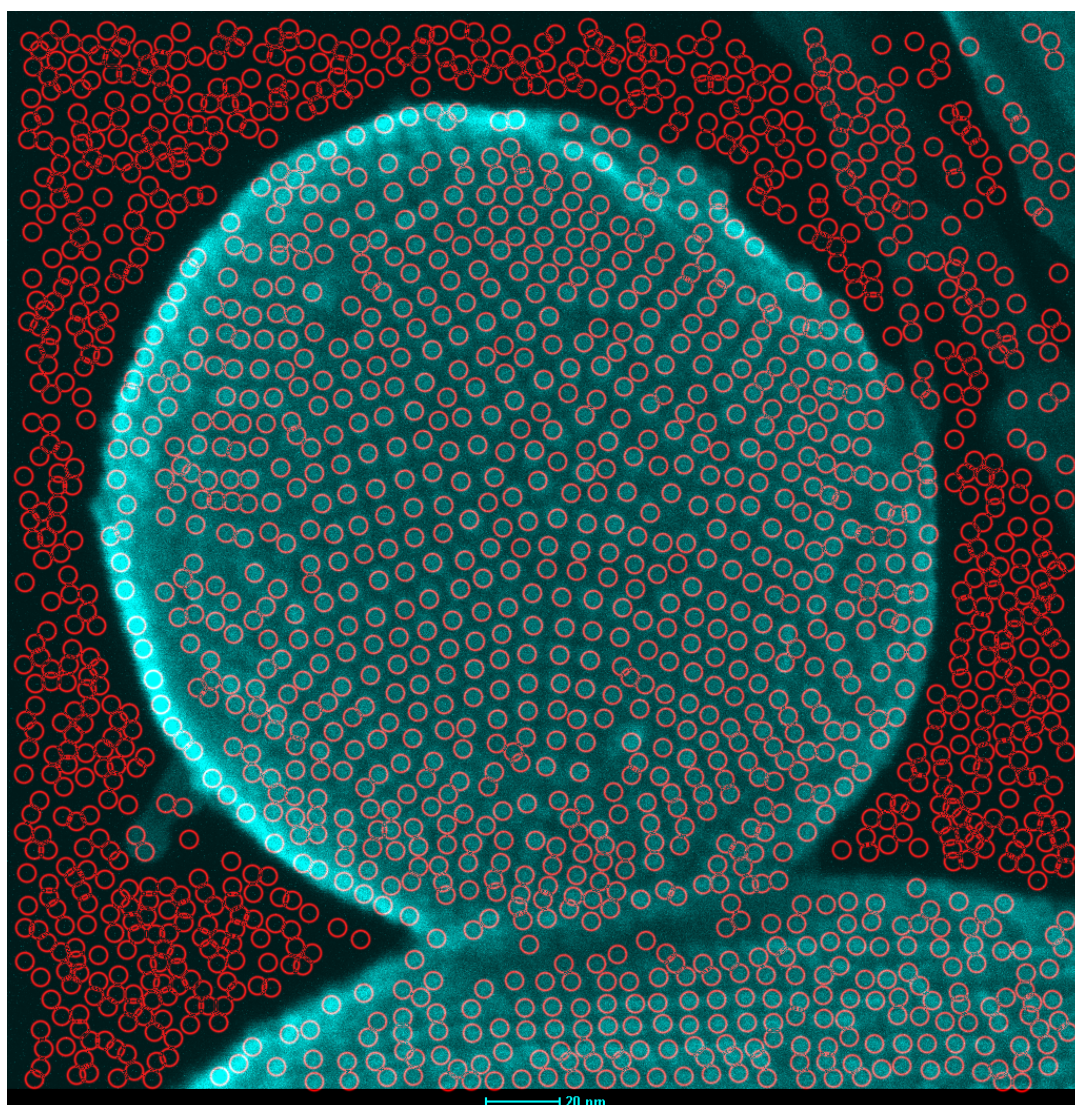
Supplementary Figure 5: Confocal images of silica colloids self-assembled into supraparticles

A plane through each assembly is shown. The different crystalline symmetry is clearly observed. **Left:** (Mackay) Icosahedral symmetry (scalebar = $5 \mu\text{m}$). **Center:** Icosahedral symmetry with anti-Mackay surface termination (scalebar = $5 \mu\text{m}$). **Right:** Large FCC crystalline domains (scalebar = $25 \mu\text{m}$). Images were Gaussian-blurred and brightness was increased to better visualize colloids.

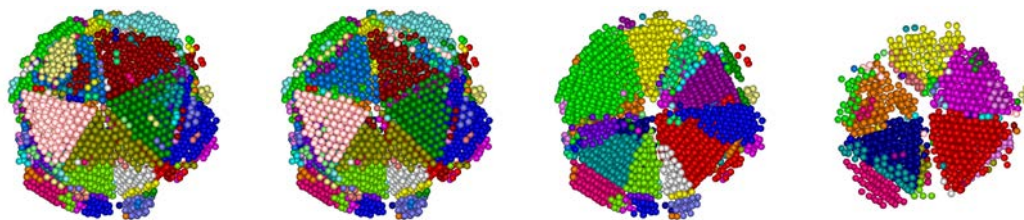


Supplementary Figure 6: Nanoparticle tracking

Determining coordinates of cobalt iron oxide nanoparticles. Particles with a red circle are recognized and their positions are determined in 3D. Those without a circle are either above/below the plane or are not recognized by the tracking software. Typical difficulties in particle tracking arose from the noise generated by the tomographic reconstruction process or due to the small gap between the particles.

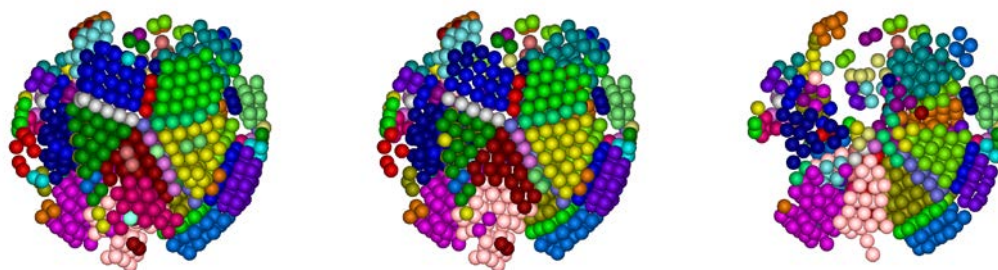


Supplementary Figure 7: Surface tracking from SE-STEM image
2D tracking of the cobalt iron oxide nanoparticles from the SE-STEM image shown in Fig. 1 (central panel). This method was used to obtain in a more accurate way the coordinates used for one of the images of Fig. 3 (bottom row, central panel).



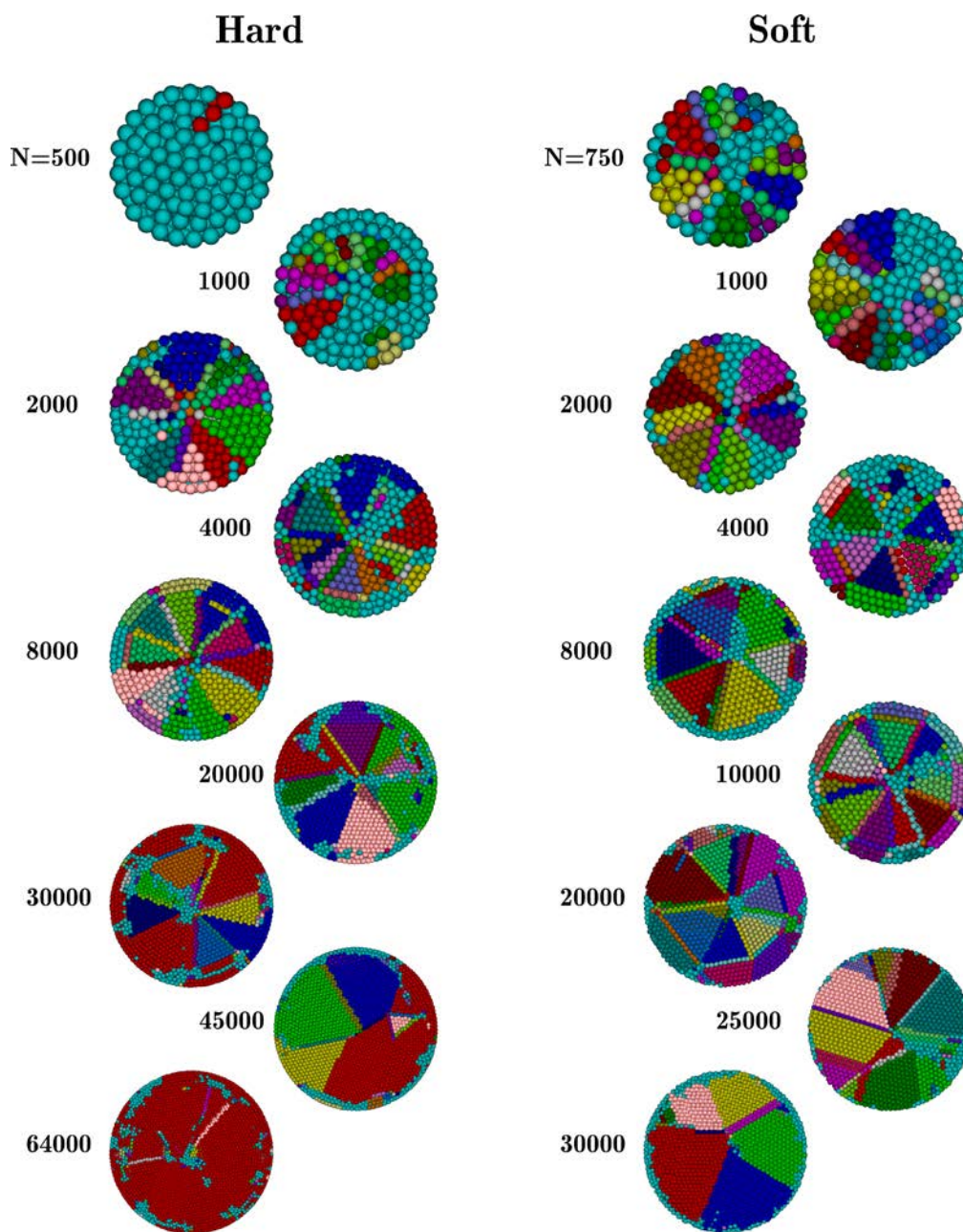
Supplementary Figure 8: Cross-sections of a nanoparticle cluster

Cuts through an icosahedral cluster of core-shell semiconductor nanoparticles. To make these figures, we obtained the 3D coordinates of the individual particles from electron micrographs using particle tracking software (8, 9). Different colors indicate different crystalline domains, as determined via a bond-orientational order parameter (10). Particles identified as non-crystalline were hidden. The first image shows the outside of the cluster, while the next three show progressively deeper cuts through the cluster, where 5, 10, and 5 tetrahedra are intersected, respectively. Note that the five-fold symmetry persists throughout the entire structure.



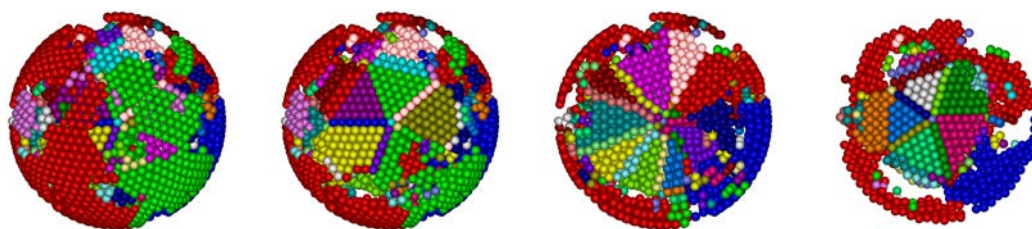
Supplementary Figure 9: Cross-sections of a colloid cluster

Cuts through an icosahedral cluster of core-shell silica colloids. To make these figures, we obtained the 3D coordinates of the individual particles from confocal microscopy images using particle tracking software (8, 9). Different colors indicate different crystalline domains, as determined via a bond-orientational order parameter (10). Particles identified as non-crystalline were hidden. The first image shows the outside of the cluster, while the other two images show cuts through the cluster, where 5 and 10 tetrahedra are intersected, respectively. Note that deeper in, the cluster is largely non-crystalline due to sedimentation effects, as mentioned in the main paper.



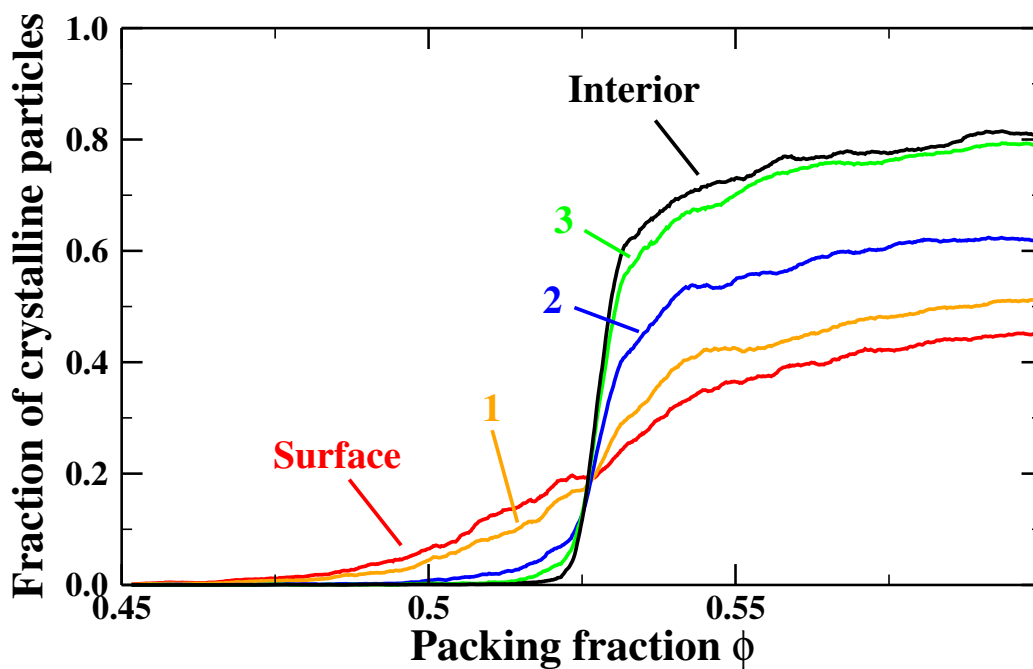
Supplementary Figure 10: Clusters from EDMD simulations

A cut through the middle of the cluster is shown for different system sizes (N is the total number of particles). **Left:** A hard spherical confinement. **Right:** A soft repulsive spherical confinement.



Supplementary Figure 11: Clusters from EDMD simulations with an attractive wall

Snapshots of a cluster of $N = 8000$ particles in a system where the wall-particle interaction was modeled by a short-ranged attractive potential. The image on the left shows the outside of the cluster, while the next three show progressively deeper cuts through the cluster, where 5, 10, and 5 tetrahedra are intersected, respectively. Particles identified as non-crystalline are hidden. Similar results were observed in smaller clusters ($N = 4000$).



Supplementary Figure 12: Crystallization process of Mackay icosahedral clusters

Crystallization process studied by event-driven molecular dynamics simulations of 2000 hard spheres in a hard spherical confinement that slowly shrinks in time. Fraction of crystalline particles in the surface layer, the first three sub-layers and the interior as a function of the packing fraction ϕ .

Supplementary Table

N	ϕ	$\Delta F = F_{\text{FCC}} - F_{\text{ico}} [k_B T/N]$
1500	0.551	0.026 ± 0.020
1500	0.571	0.036 ± 0.012
3000	0.554	0.036 ± 0.006
4000	0.537	0.030 ± 0.006
4000	0.558	0.038 ± 0.009
4000	0.572	0.034 ± 0.007

Supplementary Table 1: Free-energy differences

Free-energy difference between FCC-like and icosahedral-like arrangements of N hard spheres confined in a hard spherical cavity. Clusters with a global icosahedral symmetry are thermodynamically more stable than FCC clusters for the cluster sizes and packing fractions that are studied here.

References

1. Bodnarchuk, M. I. *et al.* Exchange-coupled bimagnetic wüstite/metal ferrite core/shell nanocrystals: Size, shape, and compositional control. *Small* **5**, 2247–2252 (2009).
2. Xie, R., Kolb, U., Li, J., Basché, T. & Mews, A. Synthesis and characterization of highly luminescent CdSe-core CdS/Zn_{0.5} Cd_{0.5}S/ZnS multishell nanocrystals. *J. Am. Chem. Soc.* **127**, 7480–7488 (2005).
3. van Blaaderen, A. & Vrij, A. Synthesis and characterization of colloidal dispersions of fluorescent, monodisperse silica spheres. *Langmuir* **8**, 2921–2931 (1992).
4. Giesche, H. Synthesis of monodispersed silica powders II. controlled growth reaction and continuous production process. *J. Eur. Ceram. Soc.* **14**, 205–214 (1994).
5. Mason, T. & Bibette, J. Shear rupturing of droplets in complex fluids. *Langmuir* **13**, 4600–4613 (1997).
6. Kremer, J. R., Mastronarde, D. N. & McIntosh, J. R. Computer visualization of three-dimensional image data using IMOD. *J. Struct. Biol.* **116**, 71–76 (1996).
7. Mastronarde, D. N. Dual-axis tomography: an approach with alignment methods that preserve resolution. *J. Struct. Biol.* **120**, 343–352 (1997).
8. Crocker, J. C. & Grier, D. G. Methods of digital video microscopy for colloidal studies. *J. Colloid Interface Sci.* **179**, 298–310 (1996).
9. Dassanayake, U., Fraden, S. & van Blaaderen, A. Structure of electrorheological fluids. *J. Chem. Phys.* **112**, 3851–3858 (2000).
10. Steinhardt, P. J., Nelson, D. R. & Ronchetti, M. Bond-orientational order in liquids and glasses. *Phys. Rev. B* **28**, 784–805 (1983).

11. ten Wolde, P. R., Ruiz-Montero, M. J. & Frenkel, D. Numerical calculation of the rate of crystal nucleation in a lennard-jones system at moderate undercooling. *J. Chem. Phys.* **104**, 9932–9947 (1996).
12. Rapaport, D. C. The Event-Driven Approach to N-Body Simulation. *Progr. Theoret. Phys. Suppl.* **178**, 5–14 (2009).
13. Schilling, T. & Schmid, F. Computing absolute free energies of disordered structures by molecular simulation. *J. Chem. Phys.* **131**, 231102 (2009).
14. Marechal, M. & Dijkstra, M. Stability of orientationally disordered crystal structures of colloidal hard dumbbells. *Phys. Rev. E* **77**, 061405 (2008).